Supporting Information

Hierarchical Zr-doped Fe_2O_3 photoanodes decorated with *in situ* Au nanoparticles via a surfactant-assisted one-step hydrothermal approach for efficient photoelectrochemical water splitting

Periyasamy Anushkkaran,[§a] Mahadeo A. Mahadik,[§b] Weon-Sik Chae,[c] Hyun Hwi Lee,[d] Sun Hee Choi*[d] and Jum Suk Jang*[ab]

[a]Department of Integrative Environmental Biotechnology, College of Environmental and Bioresource Sciences, Jeonbuk National University, Iksan, 54596, Republic of Korea

[b]Division of Biotechnology, College of Environmental and Bioresource Sciences, Jeonbuk National University, Iksan, 54596, Republic of Korea

[c]Daegu Center, Korea Basic Science Institute, Daegu 41566, Republic of Korea

[d]Pohang Accelerator Laboratory (PAL), Pohang University of Science and Technology, (POSTECH), Pohang 37673, Republic of Korea

[§]These authors contributed equally to this work.

*Corresponding authors:

E-mail address: shchoi@postech.ac.kr (S. H. Choi), jangjs75@jbnu.ac.kr (J. S. Jang)

Deposition of $NiCo(OH)_x$ cocatalyst on Zr-HT/CTAB/Au photoanode

The $NiCo(OH)_x$ deposition was done with a few changes to the literature.[1] Briefly, the as-prepared Zr-HT/CTAB/Au photoanode was immersed in a 50 mM $NiSO_4.6H_2O$ and 50 mM $Co(NO_3)_2.6H_2O$ precursor solution for 1 h at room temperature in an air-tight chamber for the formation of the $NiCo(OH)_x$ on the surface of the Zr-HT/CTAB/Au photoanode. Subsequently, the immersed sample was taken out, rinsed in deionized water and dried at 70 ºC for 10 min in a vacuum oven. The as-obtained sample was further named Zr-HT/CTAB/Au:NCH.

Characterization

The morphology of all samples was observed using high-resolution field-emission scanning electron microscopy (HR FE-SEM, Hitachi SU8230, Korean Basic Science Institute). In order to examine the purity and crystallinity of as-synthesized photoanode samples, synchrotron X-ray diffraction (SR-XRD) measurements were conducted at the BL5A beamline of PLS-II (Pohang Light Source II) in Korea. X-ray photoelectron spectroscopy (XPS) measurements were performed on a PHI Quantera II spectrometer using a monochromatic AlKα X-ray source (Chungbuk National University) and the binding energy was calibrated by the adventitious carbon peak of C 1s at 284.8 eV. For the structure in short-range order, extended X-ray absorption fine structure (EXAFS) measurements were performed for the K-edges of Fe (E_0=7,112 eV) at the BL7D beamline of PLS-II. Incident X-ray beam (I_0) monochromatized using a Si(111) double-crystal monochromator, was detuned by 25% in order to minimize the higher harmonics, and monitored with a He-filled IC SPEC ionization chamber. The fluorescence signal (I_F) from the sample was detected by the Lytle-type detector equipped with a PIPS (passivated implanted planar silicon) diode. The obtained spectra (I_F/I_0 *vs.* Energy) were background-removed, normalized, Fourier-transformed, and fitted by using ATHENA and ARTEMIS in the IFEFFIT suite of programs, and theoretical FEFF 9 code.[2,3] The high-resolution transmission electron microscopy (HR-TEM, Center for University-wide Research Facilities CURF at Jeonbuk National University) observations were carried out to illustrate the microstructure of the photoanode. The optical properties of the as-prepared photoanodes were evaluated by ultraviolet-visible absorption spectra using a UV-Vis spectrophotometer (UV-2600, Shimadzu). The bandgap of the photoanode was determined from an indirect transition of the Tauc method:

$$(\alpha h\upsilon)^{1/n} = A(h\upsilon - E_g) \quad \text{(S1)}$$

where, α is the absorption coefficient, h is Planck's constant, v is the photon frequency, A is a proportionality constant, E_g is the optical bandgap, and n is an exponent that depends on the nature of the electronic transitions. Since hematite is an indirect bandgap semiconductor, the value of $1/n$ is 1/2. The light harvesting efficiency (LHE; defined as the ratio of absorbed light to the incident light) of each photoanode can be calculated from the UV-Vis absorbance spectra:[4]

$$LHE = 1 - 10^{-A(\lambda)} \quad \text{(S2)}$$

The time-resolved photoluminescence (TR-PL) study was carried out using a confocal microscope (MicroTime-200, Picoquant, Germany) with a 40× objective. The lifetime measurements were performed at the Korea Basic Science Institute (KBSI), Daegu Center, Korea. A single-mode pulsed diode laser (470 nm with a pulse width of ~30 ps and an average power of ~80 μW) was used as an excitation source. A dichroic mirror (490 DCXR, AHF), a long-pass filter (HQ500lp, AHF), a 150 μm pinhole, and a single photon avalanche diode (PDM series, MPD) were used to collect emission from the samples. A time-correlated single-photon counting system (PicoHarp300, PicoQuant GmbH, Germany) was used to count emission photons. PL lifetime images consisting of 250×250 pixels were recorded using the time-tagged time-resolved (TTTR) data acquisition method. Exponential fitting for the obtained emission decays was accomplished using the Symphotime-64 software (Ver. 2.2). Steady-state PL spectrum was recorded in the spectral range of 490–720 nm under 470 nm laser excitation by guiding emission photons through an optical fiber to the external spectrometer (F-7000, Hitachi).

The time-resolved PL intensity is defined by,

$$I(t) = \sum A_i e^{-t/\tau_i} \quad \text{(S3)}$$

where, $I(t)$ is the PL intensity as a function of time, A is the amplitude, τ is the PL lifetime, and i is the subcomponent number of a lifetime (1–3). The intensity-weighted average lifetime $< \tau >$ is defined as follows:[5]

$$< \tau > = \sum A_i \tau_i^2 / \sum A_i \tau_i \quad \text{(S4)}$$

Photoelectrochemical (PEC) measurements

PEC measurements were performed with an Ivium CompactStat potentiostat (Ivium Instruments, The Netherlands) in a three-electrode electrochemical cell using the prepared α-Fe_2O_3 as the working electrode, Pt wire as the counter electrode and Hg/HgO as the reference electrode. An aqueous solution of 1 M NaOH (pH = 13.6) was used as the electrolyte. Current density-potential characteristics were measured by an Ivium CompactStat potentiostat with illumination using a solar simulator with the standard global solar light (AM 1.5G, 100 mW/cm^2). The potential was calculated against the reversible hydrogen electrode (RHE) by using the following Nernst equation:[6]

$$E_{RHE} = E_{Hg/HgO} + 0.059pH + E^{0}_{Hg/HgO} \quad \text{(S5)}$$

$$(E^{0}_{Hg/HgO} = 0.095\ V \text{ at } 25\ ^{0}C)$$

Current density-potential curves were obtained from 0.3 to 1.7 V *vs.* RHE with a scan rate of 50 mV/s[1]. The Nyquist plots calculated from electrochemical impedance spectroscopy (EIS) were measured at 1.23 V *vs.* RHE over the frequency range from 3000 kHz to 0.5 Hz under a 1-sun illumination condition. The Mott-Schottky plots were measured in dark conditions at a frequency of 100 Hz to understand the donor density (N_D) and flat band potential based on the following equation:[7]

$$1/C^2 = \frac{2}{q\varepsilon\varepsilon_0 N_D A^2}(V - E_{FB} - k_B T/q) \quad \text{(S6)}$$

where, q is the electron charge (1.602×10^{-19} C), ε is the dielectric constant of hematite (80), ε_0 is the permittivity of vacuum (8.854×10^{-12} F m^{-1}), E_{FB} is the flat band potential, k_B is the Boltzmann constant (1.38×10^{-23} J K^{-1}), T is the temperature and C is the capacitance derived from the electrochemical impedance obtained at each potential (V). The intensity-modulated photocurrent spectroscopy (IMPS) study was performed using a blue LED by a frequency-response analyzer with a peak wavelength of 460 nm. The average transport time of the photogenerated electron (τ_{et}) can be calculated from the angular frequency of the minimum given by the following equation:[8]

$$\tau_{et} = (2\pi f_{min})^{-1} \quad \text{(S7)}$$

where, f_{min} is the frequency at the minimum imaginary component in the IMPS semicircle. The bulk charge separation efficiency (η_{bulk}) and surface charge separation efficiency ($\eta_{surface}$) of as-synthesized photoanodes were measured by the addition of 0.5 M H_2O_2 in 1 M NaOH

electrolyte solution. The photocurrent density in the presence of H_2O_2 could represent the number of separated charges that successfully reach the electrode surface without recombination in the bulk since H_2O_2 has a faster oxidation rate and a lower overpotential than that of H_2O. The η_{bulk} and $\eta_{surface}$ were calculated by the following equations:[9]

$$J_{H_2O} = J_{abs} \times \eta_{bulk} \times \eta_{surface} \quad \text{(S8)}$$

$$J_{H_2O_2} = J_{abs} \times \eta_{bulk} \quad \text{(S9)}$$

$$\eta_{bulk} = J_{H_2O_2}/J_{abs} \times 100 \quad \text{(S10)}$$

$$\eta_{surface} = J_{H_2O}/J_{H_2O_2} \times 100 \quad \text{(S11)}$$

where, J_{H_2O} is the measured photocurrent density, J_{abs} is the photon absorption expressed as a current density (i.e., absorbed photon-to-current efficiency APCE =100%), and $J_{H_2O_2}$ is the photocurrent density in the presence of H_2O_2. The incident photon-to-current efficiency (IPCE) is measured using a CS130 monochromator (Mmac-200, Spectro) with a 300 W Xe arc lamp in the range from 350 nm to 700 nm at 1.23 V *vs*. RHE. The IPCE of as-prepared photoanodes was calculated using the following equation:[10]

$$IPCE\ (\%) = (1240 \times J_{photo})/(I_{inc} \times \lambda) \times 100\ \% \quad \text{(S12)}$$

where, J_{photo} is the measured photocurrent density at each corresponding wavelength (mA/cm^2) at 1.23 V *vs,* RHE, I_{inc} is the incident monochromatic light power density of each corresponding wavelength (mW/cm^2) and λ is the wavelength of monochromatic light (nm) respectively. The absorbed photon-to-current efficiency (APCE) is calculated using eqn. (S13):[11]

$$APCE = IPCE/LHE \quad \text{(S13)}$$

PEC water splitting

The PEC water splitting (H_2 and O_2 gases evolution) was conducted in a specially designed PEC three-electrode reactor. The working electrode as a photoanode (Zr-HT/CTAB/Au:NCH), counter electrode as Pt wire and reference electrode as Hg/HgO electrodes were mounted in an airtight glass reactor that contained a quartz-glass window to

allow light illumination without any obstacle. An aqueous solution of 1 M NaOH of pH 13.6 was filled in a reactor as an electrolyte and before the reaction started, the reactor was purged with N_2 gas (99.9%) for 2 h to remove dissolved oxygen. The amounts of H_2 and O_2 evolved were determined by a gas chromatography (GC) system equipped with a thermal conductivity detector (GC-TCD, Agilent 7820, USA) and a 5 Å molecular sieve column under 1-sun illumination (AM 1.5G, 100 mW/cm^2) condition at 1.23 V_{RHE}.

Table S1. The structural parameters calculated from nonlinear EXAFS fits for the first peak at 0.6–2.0 Å for Zr-HT, Zr-HT/CTAB, and Zr-HT/CTAB/Au photoanodes.

Sample	CN_{tot}		R_1 (Å)[c]	R_2 (Å)[d]	σ^2 ($\times 10^3$ Å^2)[e]	R-factor (%)[f]
	CN_1[a]	CN_2[b]				
Zr-HT	5.1		1.93	2.09	3.2	0.04
	3.0*	2.1				
Zr-HT/CTAB	5.1		1.93	2.08	4.5	0.02
	3.0*	2.1				
Zr-HT/CTAB/Au	5.1		1.93	2.09	3.0	0.03
	3.0*	2.1				

[a,b] Fe–O coordination number (uncertainty< 20%), *fixed parameter, $CN_{tot} = CN_1 + CN_2$
[c,d] Fe–O bond distance (uncertainty< ±0.005 Å)
[e] Debye-Waller factor (uncertainty< ±0.0004 Å^2)
[f] A measure of absolute misfit between data and theory

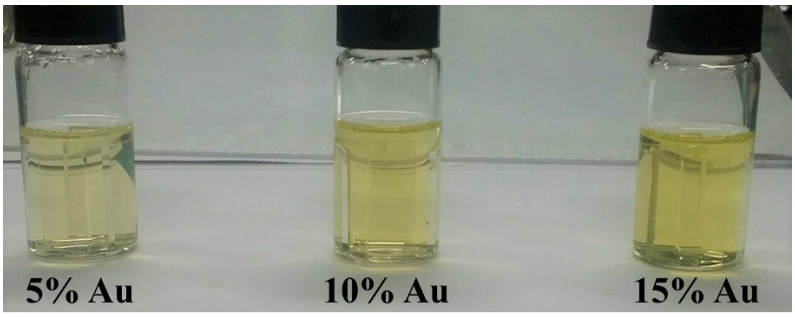

Fig. S1. Images of 5, 10 and 15% *in situ* Au incorporated Zr-doped FeOOH samples.

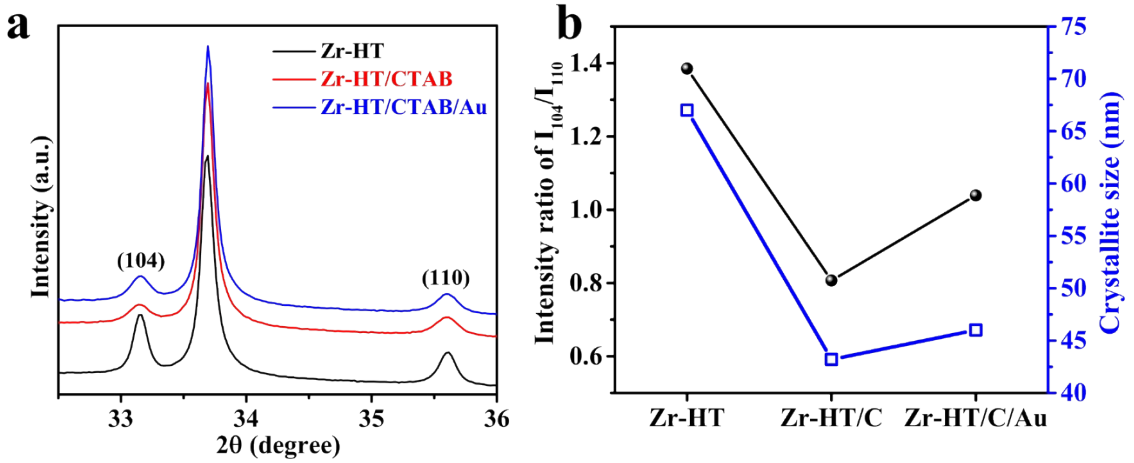

Fig. S2. (a) Diffraction profiles near the (104) and (110) peaks and (b) integrated intensity ratio (solid circles) of (104) normalized by (110) peak and the crystallite size (dashed blue squares) obtained from the (104) peak width.

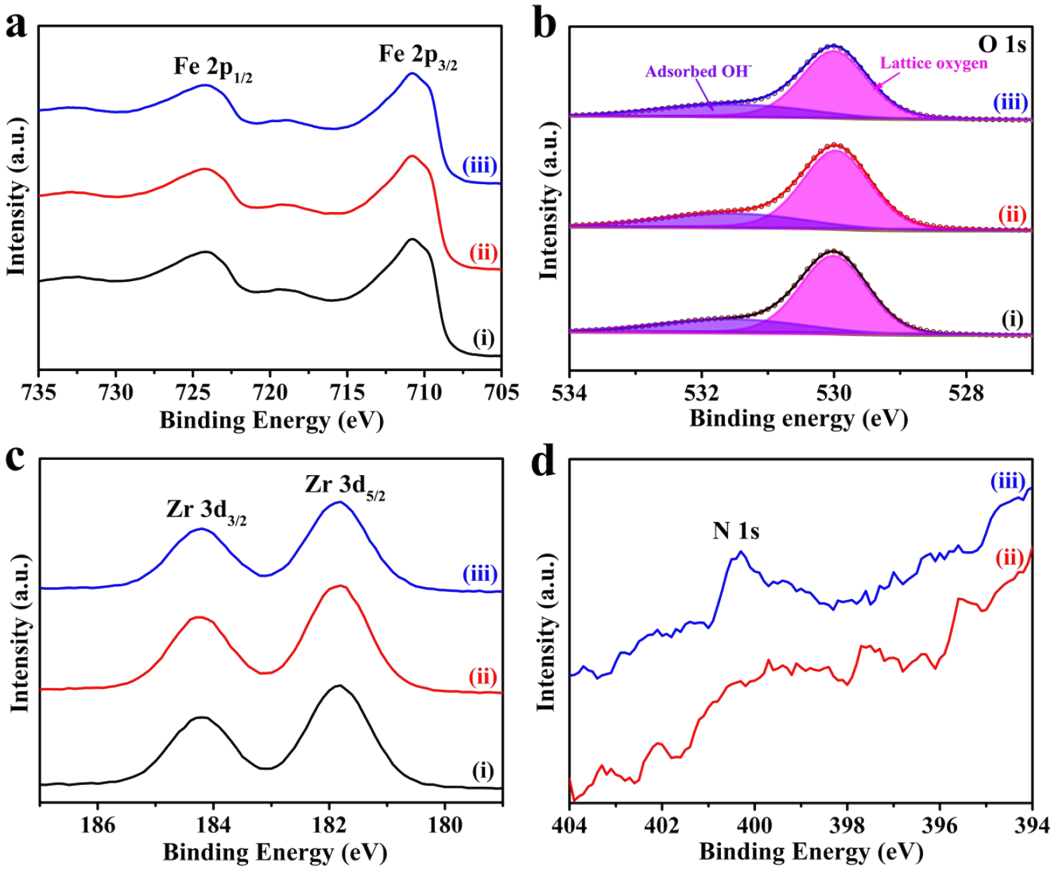

Fig. S3. XPS narrow scan spectra of (a) Fe 2p, (b) O 1s, (c) Zr 3d, and (d) N 1s peaks of (i) Zr-HT, (ii) Zr-HT/CTAB and (iii) Zr-HT/CTAB/Au photoanodes.

Fig. S3a shows two distinctive peaks located at 710.8 and 724.2 eV, originating from Fe $2p_{3/2}$ and Fe $2p_{1/2}$, respectively, accompanied by two satellite peaks at the binding energies of 719 and 733.1 eV, which were in accordance with the Fe^{3+}.[12] As shown in Fig. S3c, the Zr 3d is centered at BEs of 181.8 and 184.2 eV, which were related to Zr $3d_{5/2}$ and Zr $3d_{3/2}$, respectively, arising from typical Zr^{4+} values and demonstrating that the Zr had been doped successfully in all the studied photoanodes.[13]

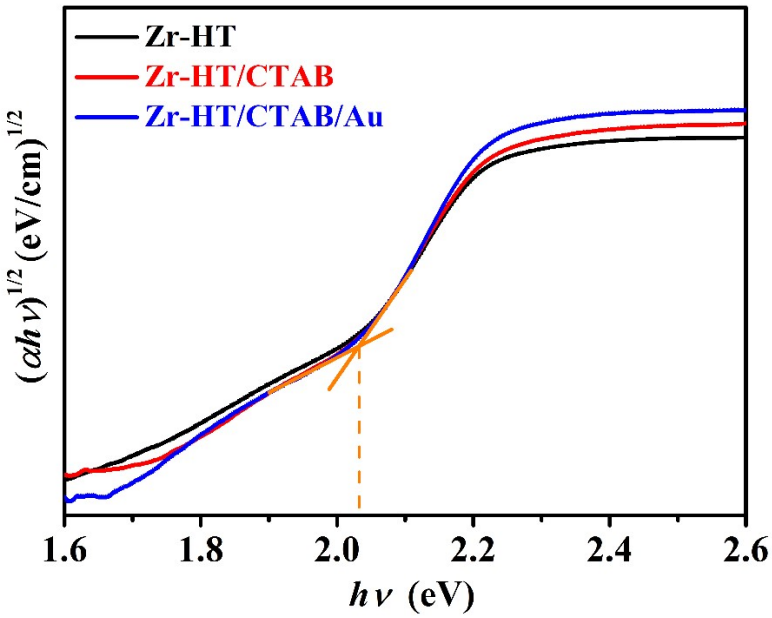

Fig. S4. Tauc plots of the Zr-HT, Zr-HT/CTAB and Zr-HT/CTAB/Au photoanodes.

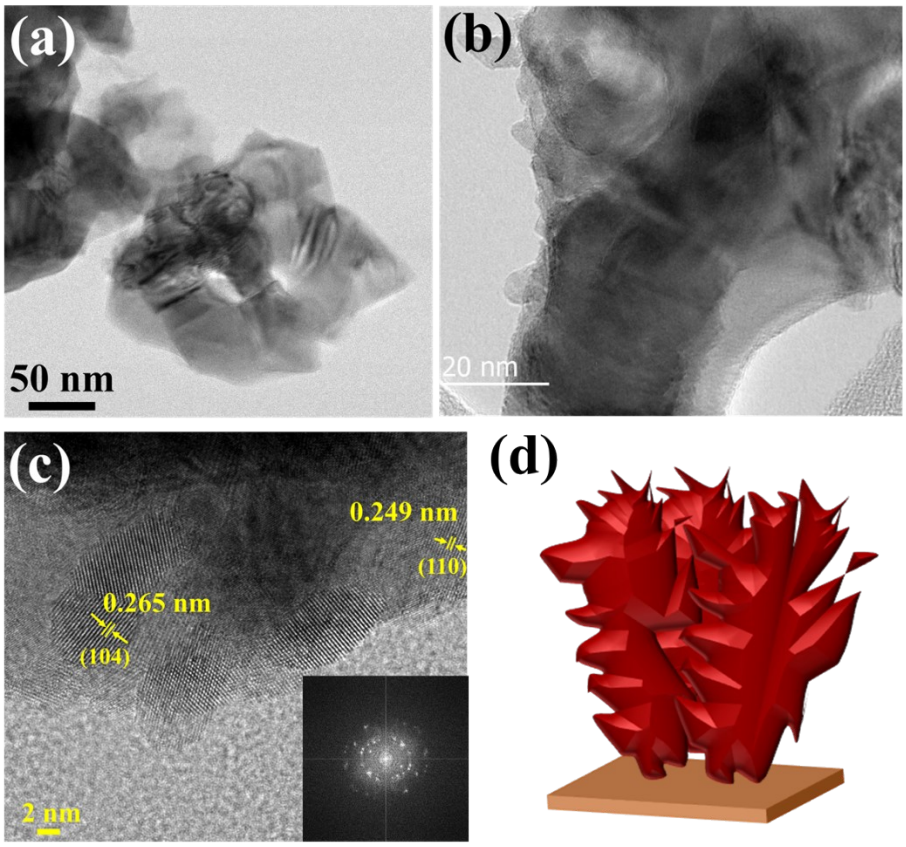

Fig. S5. (a and b) TEM and (c) HR-TEM image of Zr-HT photoanode (inset: corresponding FFT patterns); and (d) schematic illustrations of Zr-HT photoanode.

As shown in Fig. S5c, the lattice spacings of 0.249 and 0.265 nm match the (110) and (104) crystal planes of hematite, respectively.

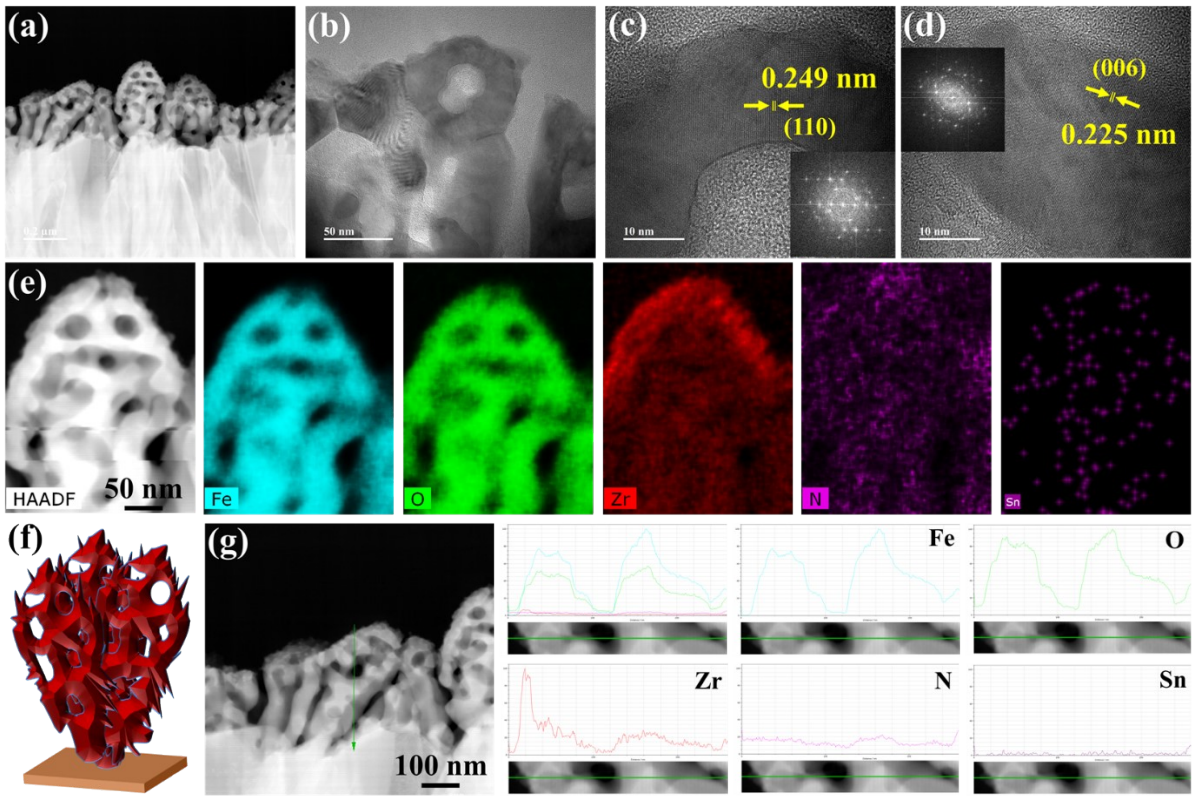

Fig. S6. (a and b) Focused ion beam-low magnification TEM images, (c and d) HR-TEM images (inset: corresponding FFT patterns); and (e) STEM-EDS elemental mapping, (f) schematic illustration and (g) TEM-EDS line profile of the Zr-HT/CTAB photoanode.

The HR-TEM images revealed a hematite with a well-organized structure, exhibiting lattice fringes of 0.249 and 0.225 nm, which agree with the (110) and (006) planes of Fe_2O_3, respectively (Fig. S6c and d). Additionally, the EDS mapping images clearly demonstrate the presence of Fe, O, Zr and N elements dispersed throughout the photoanode (Fig. S6e). In addition, it is evident that Sn was dispersed from the FTO substrate. Fig. S6f depicts the schematic of the porous structure of the Zr-HT/CTAB photoanode. Fig. S6g illustrates the TEM-EDS line scanning.

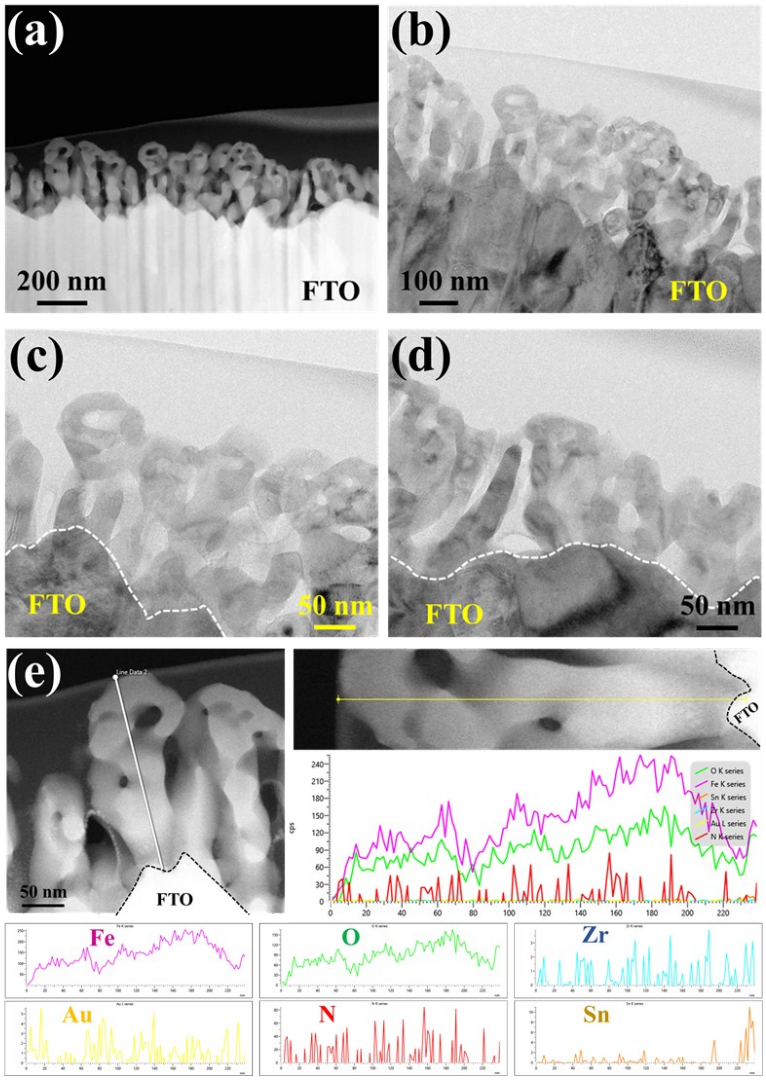

Fig. S7. (a–d) Focused ion beam-low magnification TEM images and (e) TEM-EDS line profile of the Zr-HT/CTAB/Au photoanode.

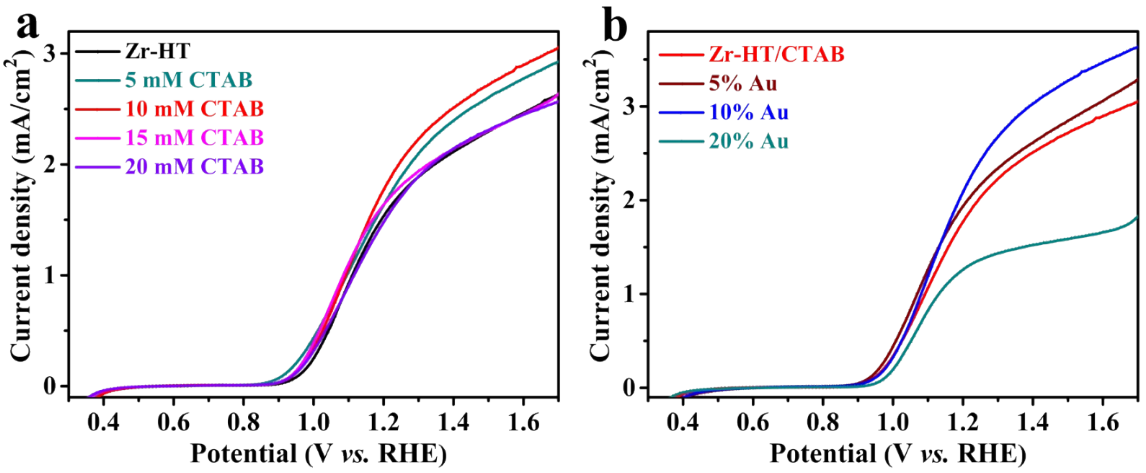

Fig. S8. *J–V* curves of (a) Zr-HT, and Zr-HT photoanode with various concentrations of CTAB and (b) Zr-HT/CTAB, and Zr-HT/CTAB photoanode with Au modification under different amounts of Au.

As illustrated in Fig. S8a, as the CTAB concentration in the precursor solution increased, the PD clearly increased. It had also been found that as CTAB surfactant increased beyond 10 mM, the PD significantly decreased. This can be due to the high CTAB concentrations may result in an environment that was highly dense and viscous, which increased diffusion resistance and was not conducive to the ordered growth of nanorods.[14,15]

As shown in Fig. S8b, a 10% Au decorated Zr-HT/CTAB photoanode achieved the highest PEC performance. As the concentration of Au increased further, the PD started to decline. This could be due to the increased Au coverage on the Zr-HT/CTAB photoanode surface, which would lower the interface between Zr-HT/CTAB/Au and electrolyte, hence, weakening the light absorption of Zr-HT/CTAB.[16]

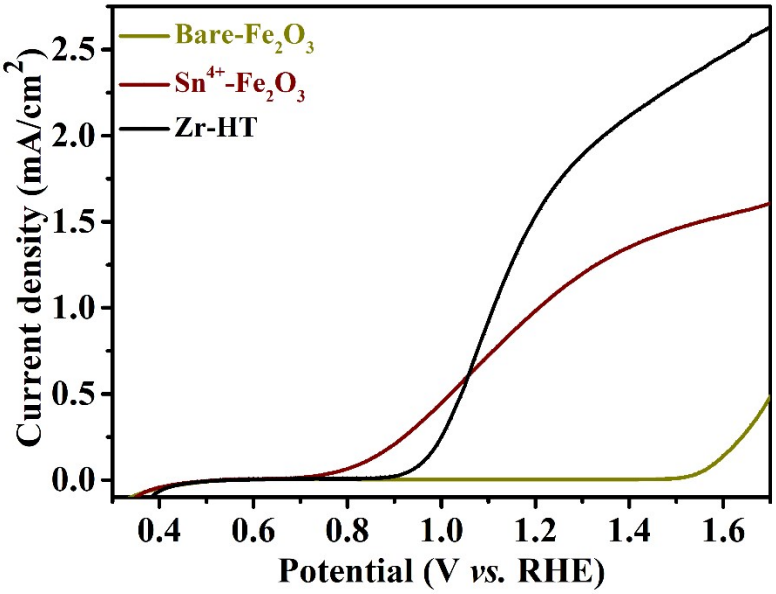

Fig. S9. *J–V* curves of Bare-Fe_2O_3, Sn^{4+}-Fe_2O_3 and Zr-HT photoanodes under 1-sun illumination.

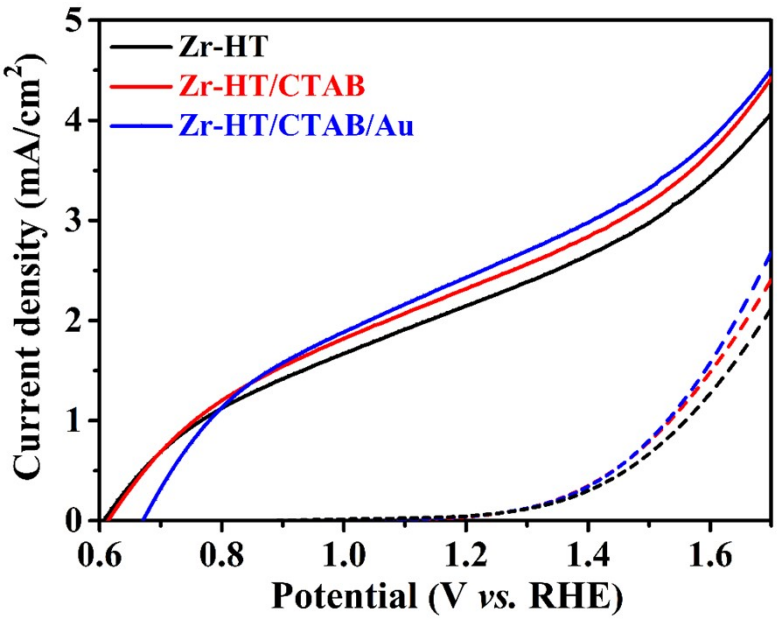

Fig. S10. *J–V* curves under light (solid lines) and dark (dashed lines) conditions for the Zr-HT, Zr-HT/CTAB and Zr-HT/CTAB/Au photoanodes using 1 M NaOH solution with 0.5 M H_2O_2 hole scavenger.

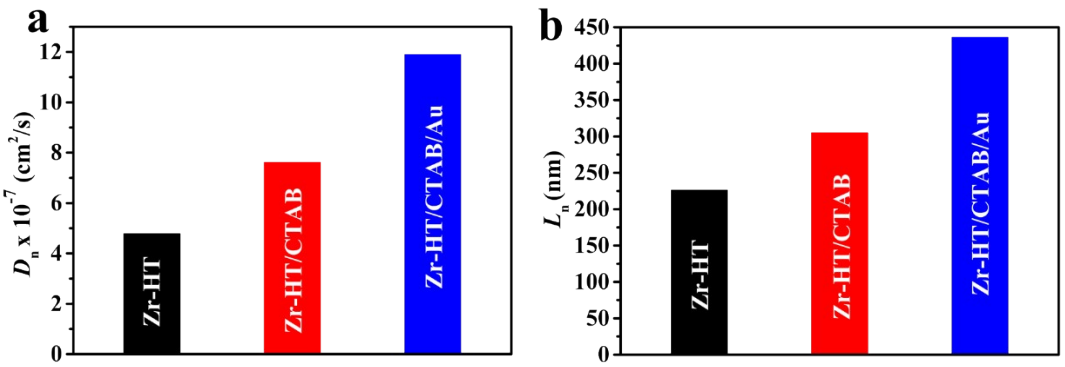

Fig. S11. (a) Electron diffusion coefficient (D_n) and (b) electron diffusion length (L_n) for Zr-HT, Zr-HT/CTAB and Zr-HT/CTAB/Au photoanodes at 1.23 V *vs.* RHE.

The electron diffusion coefficient (D_n) can be assessed from the average electron transport time (τ_{et}), which is obtained from the IMPS spectrum:[17]

$$D_n = {d^2}/{2.35\tau_{et}} \quad \text{(S14)}$$

where, d is the thickness of the film. The electron diffusion length (L_n) can be estimated using the following equation:[18]

$$L_n = \sqrt{D_n \tau_{el}} \quad \text{(S15)}$$

Table S2. Estimated values of frequency at the minimum imaginary component (f_{min}) from IMPS, average electron transport time (τ_{et}) and electron diffusion coefficient (D_n), the frequency at the maximum peak (f_{max}) from Bode plot, electron lifetime (τ_{el}) and electron diffusion length (L_n) for Zr-HT, Zr-HT/CTAB and Zr-HT/CTAB/Au photoanodes at 1.23 V *vs.* RHE.

Samples	f_{min} (Hz)	τ_{et} (ms)	D_n (cm^2/s)	f_{max} (Hz)	τ_{el} (ms)	L_n (nm)
Zr-HT	237.1	0.67	4.78×10^{-7}	149.44	1.07	226.2
Zr-HT/CTAB	315.8	0.51	7.62×10^{-7}	130.47	1.22	304.9
Zr-HT/CTAB/Au	473.2	0.34	1.19×10^{-6}	99.46	1.60	436.3

Table S3. PL lifetime parameters of the Zr-HT, Zr-HT/CTAB and Zr-HT/CTAB/Au photoanodes.

Samples	A_1 (%)	τ_1 (ns)	A_2 (%)	τ_2 (ns)	A_3 (%)	τ_3 (ns)	$<\tau>$ (ns)
Zr-HT	70.1	0.05	29.4	0.26	0.5	3.9	0.13
Zr-HT/CTAB	74.0	0.04	25.4	0.24	0.6	3.8	0.11
Zr-HT/CTAB/Au	73.3	0.04	26.1	0.24	0.6	3.3	0.11

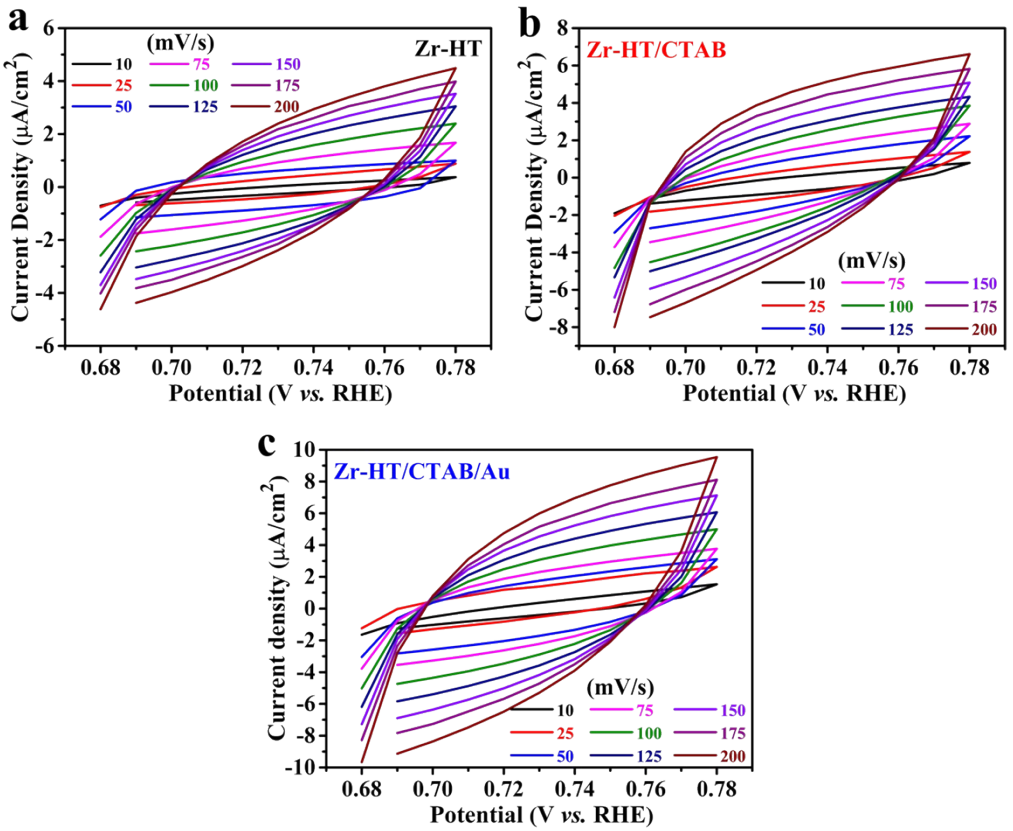

Fig. S12. Cyclic voltammograms were obtained in the non-faradaic potential region at various scan rates ranging from 10 to 200 mV/s for (a) Zr-HT, (b) Zr-HT/CTAB and (c) Zr-HT/CTAB/Au photoanodes using 1 M NaOH electrolyte.

The electrochemically active surface area (ECSA) was determined using double-layer capacitance (C_{dl}) measurements at 9 different scan rates (10, 25, 50, 75, 100, 125, 150, 175 and 200 mV/s) in the non-Faradaic region of 0.68–0.78 V_{RHE} by using cyclic voltammograms are illustrated in Fig. S12. The values of the differences between the anodic and cathodic current densities at 0.73 V_{RHE} are plotted against scan rates. The slopes of the fitting line can be used to estimate the C_{dl} of the as-prepared photoanodes, as the slope is twice the C_{dl}. The ECSA was then computed using the following formula based on the obtained C_{dl} values:[19]

$$ECSA = {}^{C_{dl}}\!/_{C_s} \qquad \text{(S16)}$$

where, C_s is the specific capacitance of the sample, which is 40 μF/cm^2 in 1 M NaOH electrolyte.

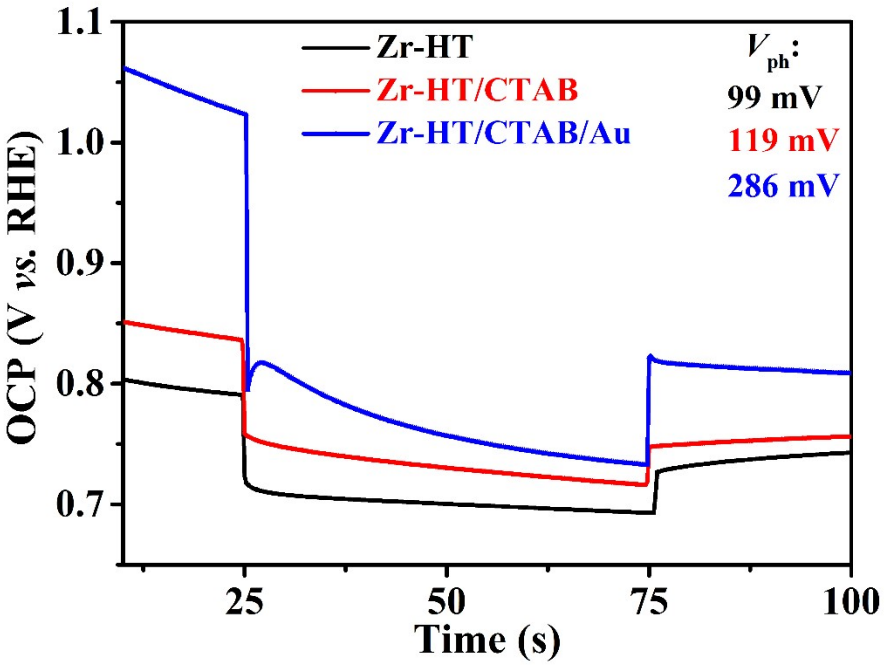

Fig. S13. OCP under dark and light illumination for Zr-HT, Zr-HT/CTAB and Zr-HT/CTAB/Au photoanodes.

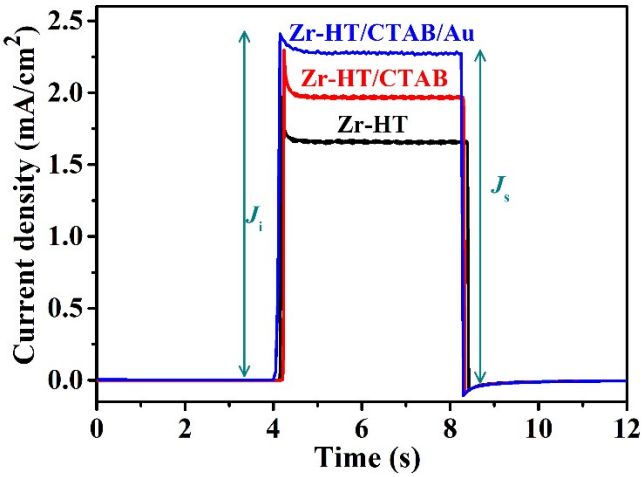

Fig. S14. Transient photocurrent response of Zr-HT, Zr-HT/CTAB and Zr-HT/CTAB/Au photoanodes measured at 1.23 V_{RHE} in 1 M NaOH electrolyte under 1-sun illumination condition.

The anodic transient time constant (τ_t) is estimated using the following equation:[20]

$$D = {}^{J_t - J_s}\!/_{J_i - J_s} \qquad \text{(S17)}$$

where, J_t denotes PD at time t, J_s is the PD after reaching the stabilization (steady state PD) and J_i is the transient anodic spike PD as depicted in Fig. S14. The transient decay time is defined as the time at which ln D = -1.

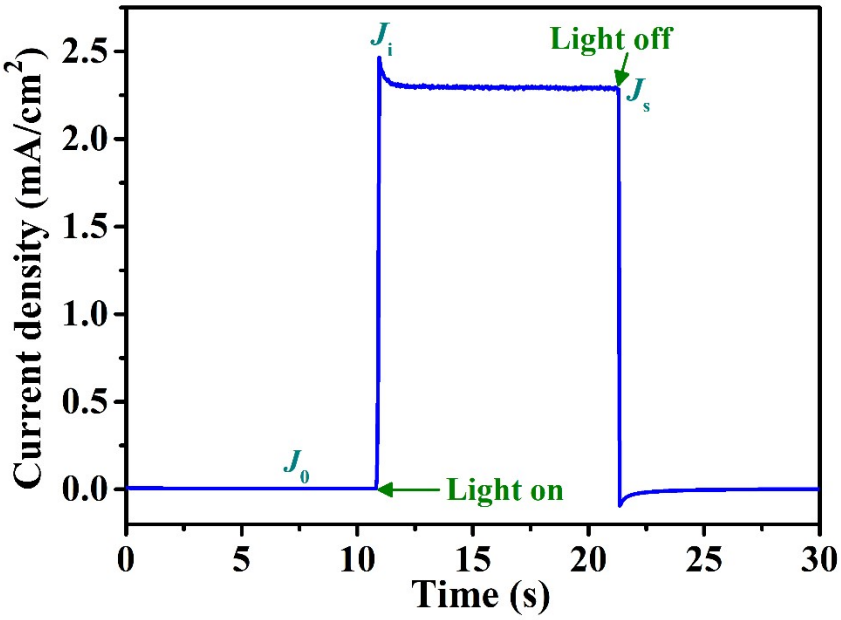

Fig. S15. An example of the current-time curve of Zr-HT/CTAB/Au photoanode at 1.23 V_{RHE} for the calculation of the relative difference between the intensities of anodic spikes and steady-state photocurrent (I_D).[21]

$$I_D = [J_i - J_s] / [J_s - J_0] \quad \text{(S18)}$$

where, J_0 is the PD in the dark.

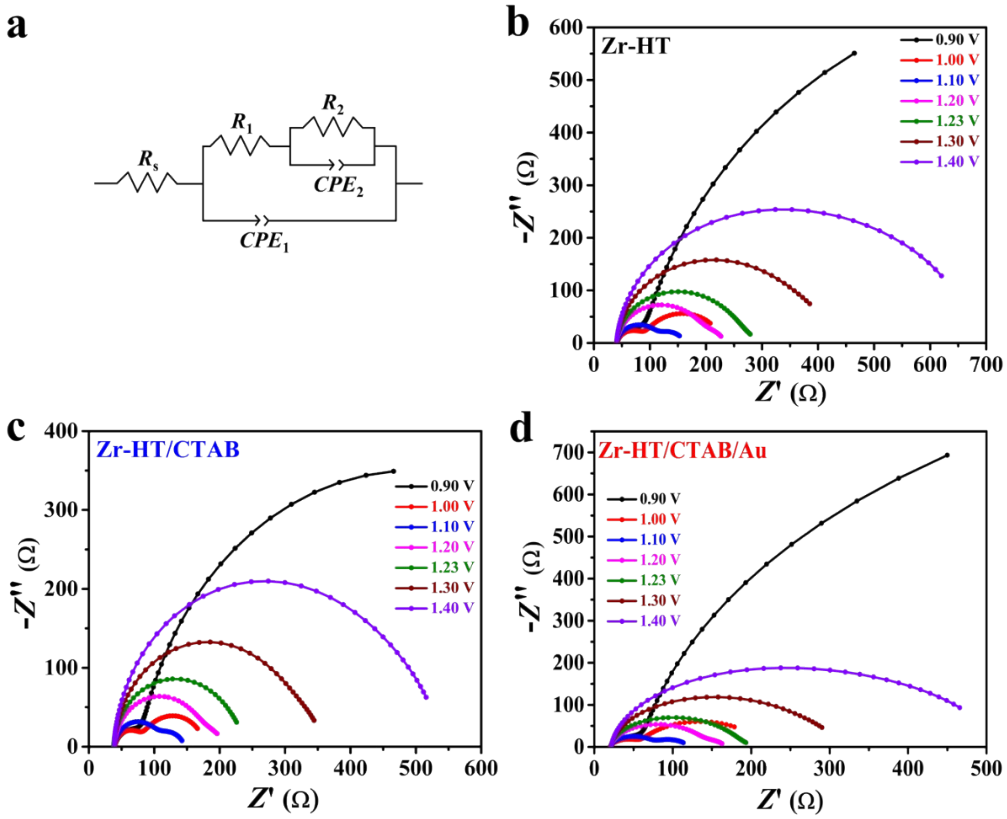

Fig. S16. (a) Corresponding equivalent circuit model for EIS data fitting, and fitted Nyquist plots obtained from EIS measurements under 1-sun illumination for the (b) Zr-HT, (c) Zr-HT/CTAB and (d) Zr-HT/CTAB/Au photoanodes at different applied potentials.

Table S4. EIS fitting parameters for Zr-HT photoanode at various applied potentials.

Potentials	R_s (Ω)	R_1 (Ω)	R_2 (Ω)	CPE_1 (μF)	CPE_2 (μF)
0.90 V	41.3	66.7	1663.0	78.2	391.9
1.00 V	41.5	43.8	145.2	46.7	956.0
1.10 V	41.1	45.0	75.5	32.6	1922.0
1.20 V	40.7	136.3	65.2	25.3	3033.6
1.23 V	41.1	184.1	69.4	22.8	2423.0
1.30 V	40.5	339.7	79.2	22.1	1209.5
1.40 V	40.7	512.1	142.4	18.8	379.2

Table S5. EIS fitting parameters for Zr-HT/CTAB photoanode at various applied potentials.

Potentials	R_s (Ω)	R_1 (Ω)	R_2 (Ω)	CPE_1 (μF)	CPE_2 (μF)
0.90 V	39.4	53.0	821.4	70.0	408.5
1.00 V	39.6	45.9	93.3	37.3	937.4
1.10 V	39.3	39.7	67.6	27.1	1787.3
1.20 V	38.8	125.3	50.8	22.3	3757.0
1.23 V	38.2	167.7	53.5	19.7	2857.5
1.30 V	38.5	280.0	34.3	19.9	1518.0
1.40 V	38.2	406.0	108.8	18.2	880.0

Table S6. EIS fitting parameters for Zr-HT/CTAB/Au photoanode at various applied potentials.

Potentials	R_s (Ω)	R_1 (Ω)	R_2 (Ω)	CPE_1 (μF)	CPE_2 (μF)
0.90 V	20.2	61.2	2174.0	100.0	295.7
1.00 V	20.3	42.4	150.8	56.7	1106.1
1.10 V	20.7	56.1	43.6	38.8	2810.0
1.20 V	21.3	110.9	38.5	26.2	4239.5
1.23 V	21.2	149.5	32.9	26.9	3689.1
1.30 V	21.3	263.4	25.0	25.7	930.5
1.40 V	21.3	421.7	50.8	23.3	417.8

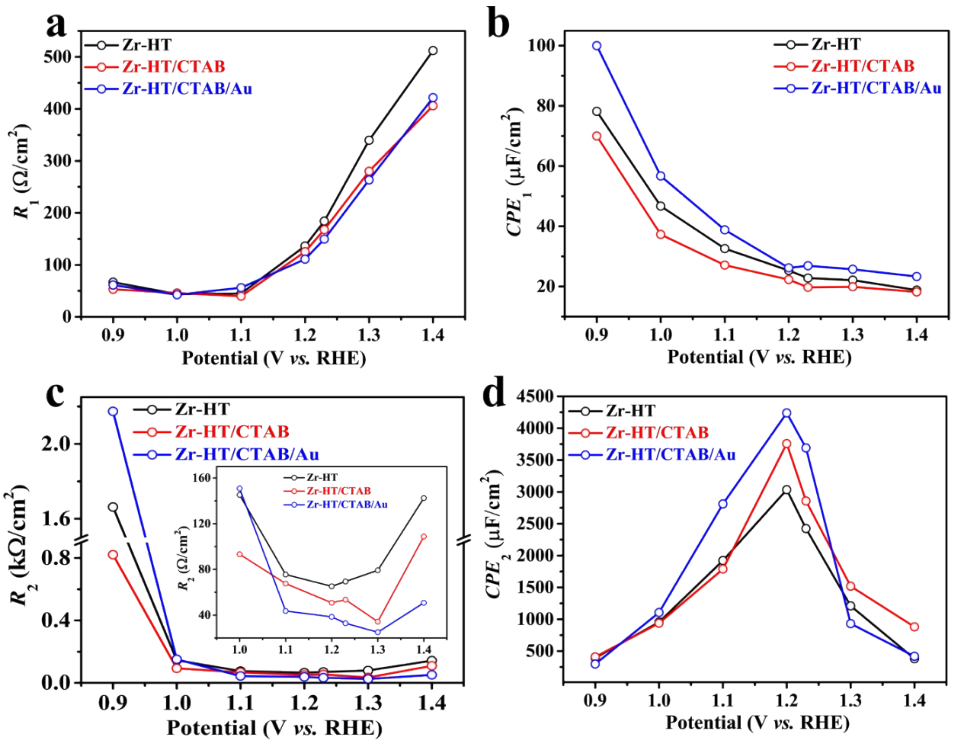

Fig. S17. Equivalent circuit fitted parameters of (a) R_1, (b) CPE_1, (c) R_2 and (d) CPE_2 values at various applied potentials were obtained from fitting EIS data for the Zr-HT, Zr-HT/CTAB and Zr-HT/CTAB/Au photoanodes.

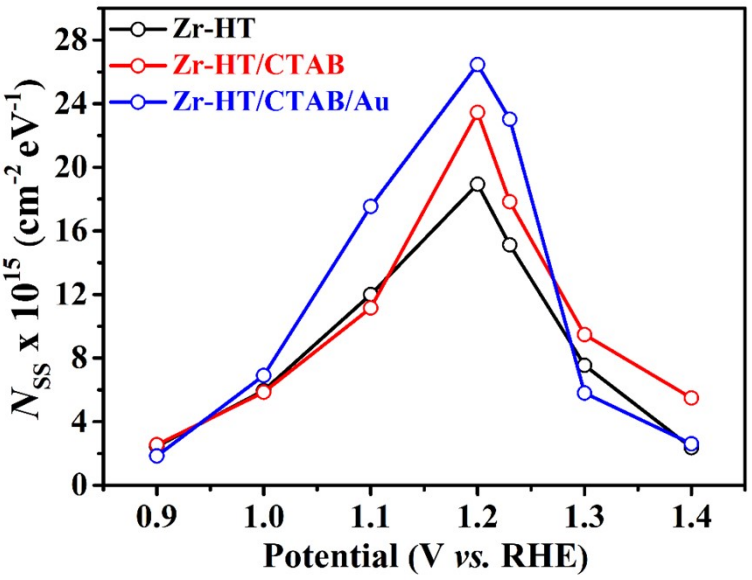

Fig. S18. Density of surface states (DOSS) as a function of the applied potential for Zr-HT, Zr-HT/CTAB and Zr-HT/CTAB/Au photoanodes.

$$\text{Density of Surface States} = CPE_2/q \qquad \text{(S19)}$$

where, q is the electron charge (1.602×10^{-19} C). The surface recombination rate constant (k_{rec}) and charge transfer rate constant (k_{ct}) were estimated using the given equations:[22]

$$\frac{k_{rec}}{k_{ct}} = \frac{R_2}{R_1} \qquad \text{(S20)}$$

$$k_{ct} = \frac{1}{R_2 CPE_2} \qquad \text{(S21)}$$

The charge transfer efficiency (η_{CT}) at the SEI is measured through the following equation:

$$\eta_{CT} = {k_{ct}}/{(k_{ct} + k_{rec})} \qquad \text{(S22)}$$

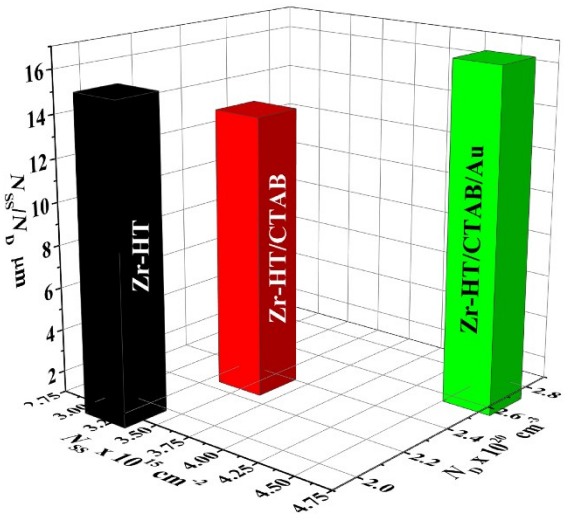

Fig. S19. Total density of surface state (N_{SS}), donor density (N_D) and their ratio (N_{SS}/N_D) for the Zr-HT, Zr-HT/CTAB and Zr-HT/CTAB/Au photoanodes.

As depicted in Fig. S19 and Table S7, the Zr-HT photoanode exhibited a higher N_{SS}/N_D ratio compared to Zr-HT/CTAB; nonetheless, it had poor PEC performance, demonstrating that a high N_{SS}/N_D ratio did not necessarily assure a high PEC activity. This can be due to the number of donors that exist in the Zr-HT being insufficient to donate a high conductivity on the photoanode.[23] In the case of the Zr-HT/CTAB photoelectrode, the porous structure assisted in diffusing more Sn, which consequently resulted in an enhancement in N_D. As well, it enabled to improve the bulk properties, which in turn, led to an increase in PEC efficiency. However, the performance of its PEC was still hindered by a lack of surface states.[24] For the Zr-HT/CTAB/Au photoanode, a sufficiently high N_{SS}/N_D ratio indicates that there were adequate N_{SS} and N_D available to further boost the photocurrent.

Table S7. The calculated N_{SS}, N_D and N_{SS}/N_D of the Zr-HT, Zr-HT/CTAB and Zr-HT/CTAB/Au photoanodes.

Samples	$N_{SS} \times 10^{15}$ (cm^{-2})	$N_D \times 10^{20}$ (cm^{-3})	N_{SS}/N_D (μm)
Zr-HT	3.02	2.01	15.03
Zr-HT/CTAB	3.28	2.44	13.44
Zr-HT/CTAB/Au	4.50	2.76	16.30

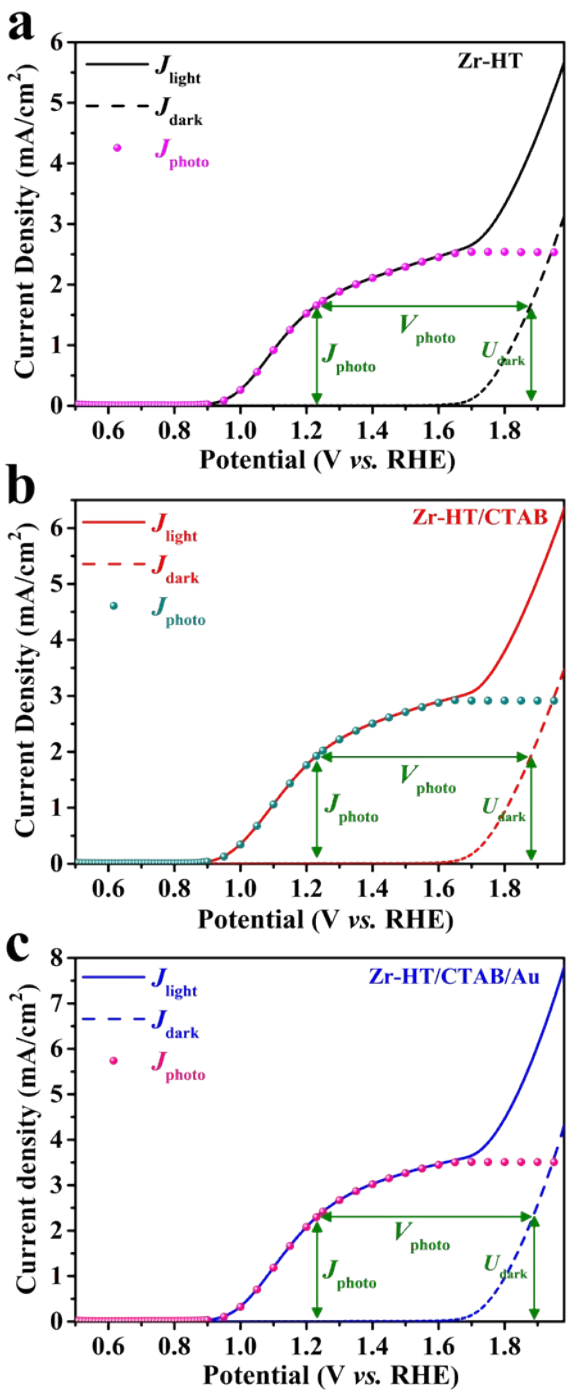

Fig. S20. *J–V* curves under simulated solar illumination (solid lines) and dark (dashed lines) and generated photocurrent (J_{photo}; symbols) of the (a) Zr-HT, (b) Zr-HT/CTAB and (c) Zr-HT/CTAB/Au photoanodes.

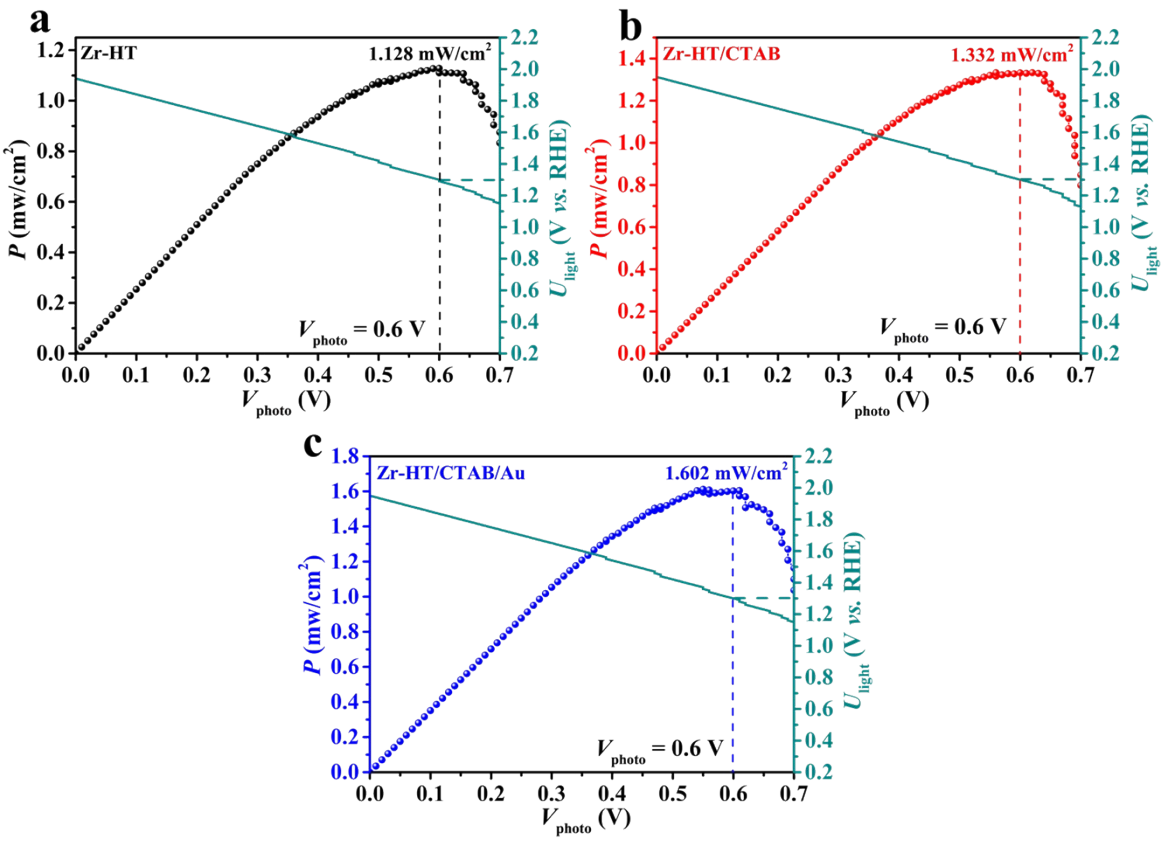

Fig. S21. Intrinsic photovoltaic power (P) as a function of photopotential for the (a) Zr-HT, (b) Zr-HT/CTAB and (c) Zr-HT/CTAB/Au photoanodes. The secondary y-axis on the right of the plots represents the potential that was applied to the photoanode under light (U_{light}).

$$P = J_{photo} \times V_{photo} \qquad \text{(S23)}$$

The secondary y-axis of these figures represents the potential applied to the photoanode under light conditions (U_{light}). As shown in Fig. S21c, the optimized Zr-HT/CTAB/Au photoanode produced a maximum electrical power of 1.602 mW/cm^2 (from solar-simulated light power of 100 mW/cm^2) at a potential of 1.3 V_{RHE}.

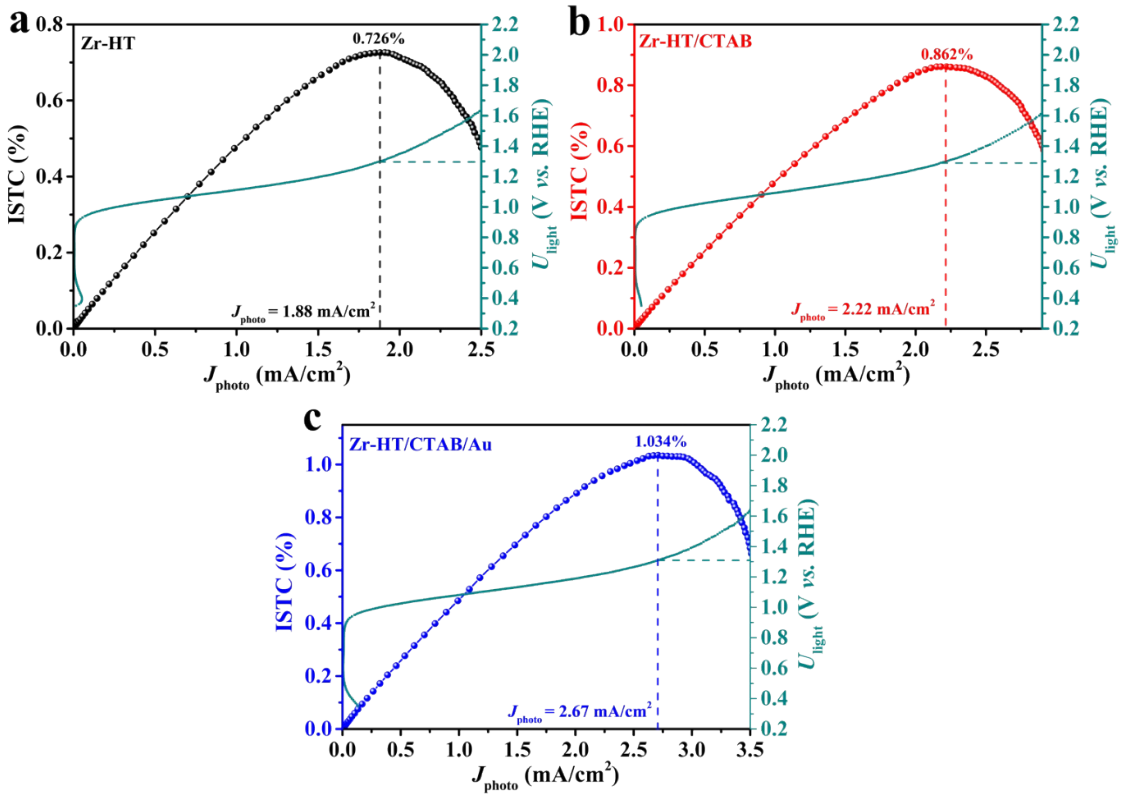

Fig. S22. ISTC efficiency as a function of the photocurrent for the (a) Zr-HT, (b) Zr-HT/CTAB and (c) Zr-HT/CTAB/Au photoanodes. The secondary *y*-axis on the right of the plots represents the potential that was applied to the photoanode under light (U_{light}).

The ISTC efficiency of the photoanode is given by the following equation:[25]

$$ISTC\ (\%) = \left[\eta_{el}\frac{J_{photo} \times V_{photo}}{P_{light}}\right]_{AM\ 1.5G} \cong \frac{1.23\ (V_{RHE})}{U_{dark}\ (V_{RHE})}\left[\frac{J_{photo}(mA/cm^2) \times V_{photo}(mA/cm^2)}{100\ (mW/cm^2)}\right] \quad \text{(S24)}$$

The Zr-HT/CTAB/Au photoanode achieved ISTC efficiency of 1.034% at a PD of 2.67 mA/cm^2 and a potential (U_{light}) of 1.3 V_{RHE} (Fig. S22c); the resulting ISTC efficiencies are 42 and 20% greater than those of the Zr-HT and Zr-HT/CTAB photoanodes, respectively. The PD of 2.67 mA/cm^2 (Fig. S22c) can be attained in both the light and dark at potentials of 1.3 V_{RHE} and 1.9 V_{RHE}, respectively, denotation that the simulated solar light power saved 0.60 V (Fig. S22c) from the external power source (i.e., 0.60 V × 2.67 mA/cm^2 = 1.602 mW/cm^2). The conversion efficiency of the electrolysis reaction (η_{el} = 1.23/U_{dark}), which is 64.7% for Zr-HT/CTAB/Au, reduced the amount of electric power saved from the power source. Hence, the Zr-HT/CTAB/Au photoanode generated 1.034 mW/cm^2 (64.7% × 1.602 mW/cm^2) of the light-induced chemical power, which is associated with an ISTC efficiency of 1.034%.

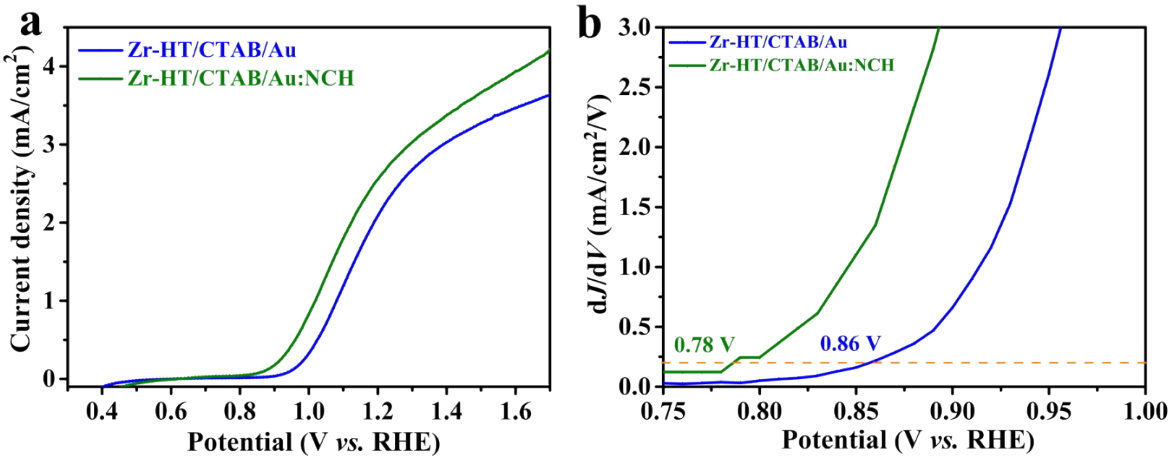

Fig. S23. (a) *J*–*V* curves under 1-sun illumination and (b) first-order derivate curves of the photocurrent densities as a function of the voltage curves of Zr-HT/CTAB/Au and Zr-HT/CTAB/Au:NCH photoanodes.

The onset potentials of as-prepared photoanodes are evaluated as the value at which the first-order derivative of the photocurrent density *vs*. potential (d*J*/d*V*) is equal to 0.2 mA cm^{-2} V^{-1}.[26] As can be observed from Fig. S23b, the Zr-HT/CTAB/Au photoanode showed an onset potential of 0.86 V_{RHE}. The onset potential of $NiCo(OH)_x$ cocatalyst-coated Zr-HT/CTAB/Au photoanode exhibited 0.78 V_{RHE}, signifying that the $NiCo(OH)_x$ accelerated the hole mobility from the photoanode to the electrolyte.

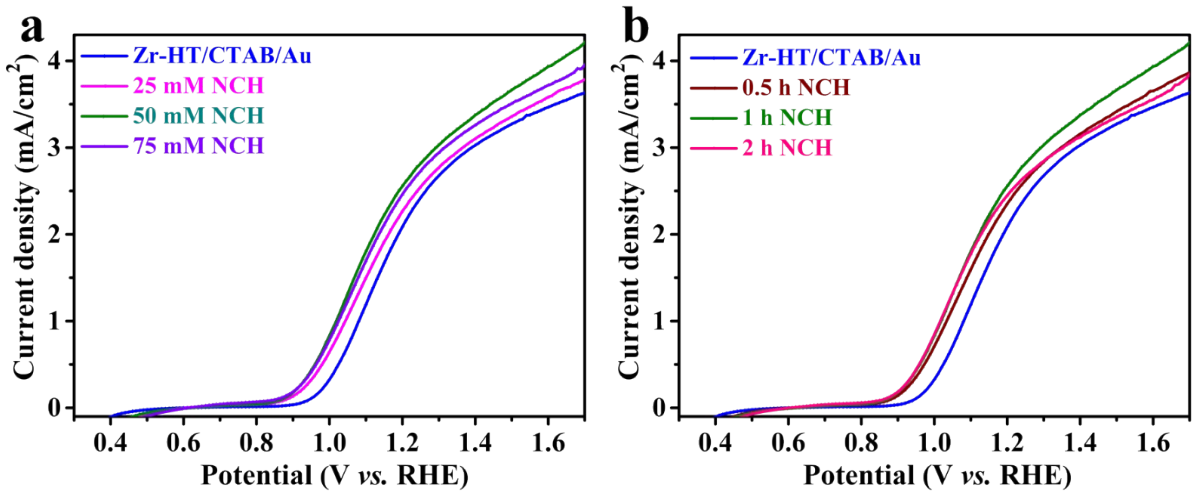

Fig. S24. *J–V* curves of Zr-HT/CTAB/Au:NCH photoanodes obtained by (a) $NiCo(OH)_x$ cocatalyst deposition in various $NiSO_4$ and $Co(NO)_3$ concentrations for 1 h and (b) $NiCo(OH)_x$ cocatalyst deposition at different times under 50 mM $NiSO_4$ and 50 mM $Co(NO)_3$ precursors (where, NCH denotes $NiCo(OH)_x$).

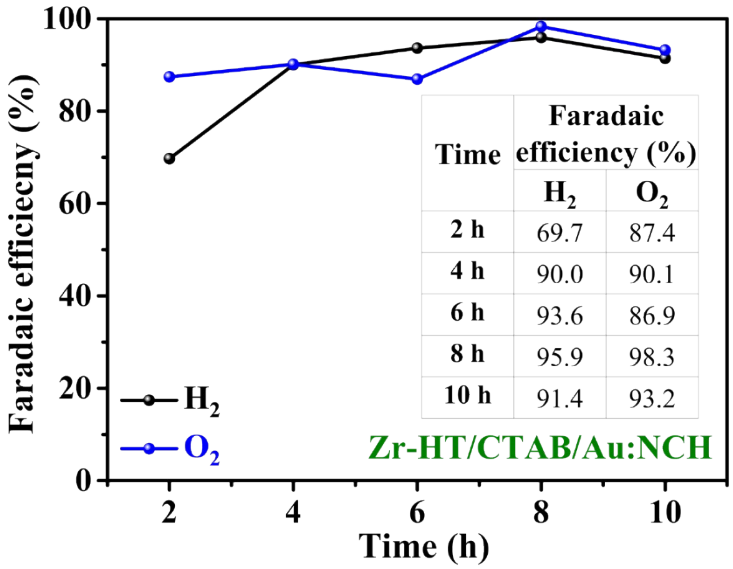

Time	Faradaic efficiency (%)	
	H_2	O_2
2 h	69.7	87.4
4 h	90.0	90.1
6 h	93.6	86.9
8 h	95.9	98.3
10 h	91.4	93.2

Fig. S25. Faradaic efficiency of Zr-HT/CTAB/Au:NCH photoanode.

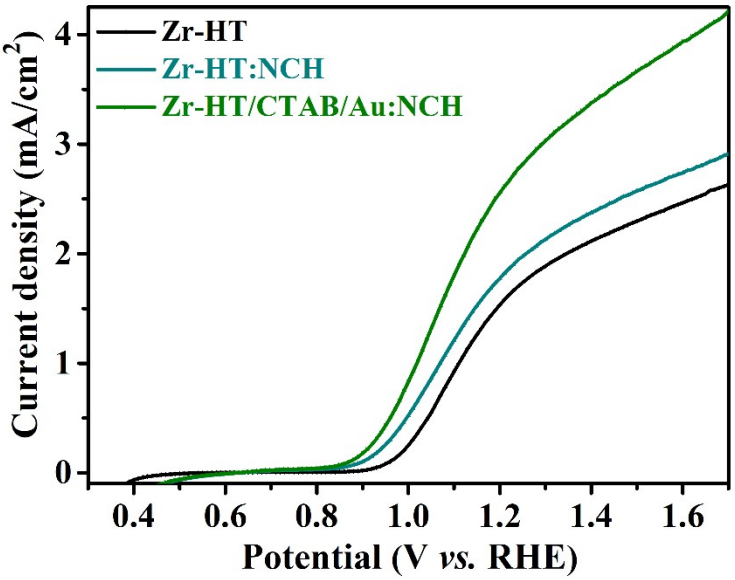

Fig. S26. *J–V* curves of Zr-HT, Zr-HT:NCH and Zr-HT/CTAB/Au:NCH photoanodes under 1-sun illumination.

Table S8. Recent literature on Zr-doped Fe_2O_3 based photoanodes for PEC water splitting.

Photoanode Materials	Photocurrent (mA/cm² at 1.23 V_{RHE})/electrolyte	Ref.
Zr-Fe_2O_3/F-FeOOH	2.11/1 M KOH	[13]
Zr/Sn co-doped Fe_2O_3	1.64/1 M NaOH	[27]
Zr/Ti co-doped Fe_2O_3	1.51/1 M NaOH	[28]
Zr-Fe_2O_3/FeF_x/FeNiOOH	1.81/1 M NaOH	[29]
Zr-Fe_2O_3/NiFe-MOF	2.19/1 M KOH	[30]
Zr-Fe_2O_3/CoCr LDH	2.02/1 M KOH	[31]
Zr/Nb co-doped Fe_2O_3/CoPi	2.36/1 M NaOH	[32]
Zr/F co-doped Fe_2O_3/CoPi	2.29/1 M NaOH	[33]
Zr-Fe_2O_3/CTAB/Au:NCH	**2.72/1 M NaOH**	**This study**

Table S9. Recent literature on Au decorated Fe_2O_3 based photoanodes for PEC water splitting.

Photoanode Materials	Au deposition method	Photocurrent (mA/cm² at 1.23 V_{RHE})/electrolyte	Ref.
Au/SiO_2:Fe_2O_3	Dropping	0.13/0.5 M Na_2SO_4	[16]
Fe_2O_3/FeOOH/Au	Dip-coating	3.20/1 M KOH	[34]
AuPt/Fe_2O_3	Spin-coating	0.83/0.5 M Na_2SO_4	[35]
Au/Fe_2O_3	Spin-coating	1.75/1 M KOH	[36]
Ti-Fe_2O_3/Al_2O_3/Au	Dropping	1.50/1 M NaOH	[37]
Au/Fe_2O_3	Dip-coating	1.20/1 M NaOH	[38]
Fe_2O_3/Au/TiO_2	Sputtering	1.05/1 M NaOH	[39]
AuPi/Fe_2O_3	Photo-deposition	1.32/1 M NaOH	[40]
Zr-Fe_2O_3/CTAB/Au:NCH	***In-situ* hydrothermal**	**2.72/1 M NaOH**	**This study**

References

1. C. Feng, B. Zhao and Y. Bi, *J. Mater. Chem. A*, 2022, **10,** 12811–12816.
2. B. Ravel and M. Newville, *J. Synchrotron Radiat.*, 2005, **12,** 537–541.
3. J. J. Rehr, J. J. Kas, F. D. Vila, M. P. Prange and K. Jorissen, *Phys. Chem. Chem. Phys.*, 2010, **12,** 5503–5513.
4. J. Huang, G. Hu, Y. Ding, M. Pang and B. Ma, *J. Catal.*, 2016, **340,** 261–269.
5. P. Anushkkaran, M. A. Mahadik, J. B. Hwang, S. Kim, W. S. Chae, H. H. Lee, S. H. Choi and J. S. Jang, *Appl. Surf. Sci.*, 2022, **592,** 153212.
6. P. Anushkkaran, T. S. Koh, W. S. Chae, H. H. Lee, S. H. Choi and J. S. Jang, *ACS Sustain. Chem. Eng.*, 2023, **11,** 5895–5907.
7. M. H. Rodrigues, I. Rodríguez-Gutiérrez, C. Ospina, C. Costa, C. A. Biffe, J. B. S. Junior, F. L. Souza and E. R. Leite, *J. Mater. Chem. A*, 2022, **10,** 13456–13466.
8. X. Zhong, H. He, J. Du, Q. Ren, J. Huang, Y. Tang, J. Wang, L. Yang, F. Dong, L. Bian and Y. Zhou, *Electrochim. Acta*, 2019, **304,** 301–311.
9. Z. Luo, C. Li, S. Liu, T. Wang and J. Gong, *Chem. Sci.*, 2017, **8,** 91–100.
10. X. Y. Yang, Z. W. Chen, X. Z. Yue, X. Du, X. H. Hou, L. Y. Zhang, D. L. Chen and S. S. Yi, *Small*, 2022, **19,** 2205246.
11. T. Shen, J. Tian, L. Lv, C. Fei, Y. Wang, T. Pullerits and G. Cao, *Electrochim. Acta*, 2016, **191,** 62–69.
12. F. Li, J. Li, L. Gao, Y. Hu, X. Long, S. Wei, C. Wang, J. Jin and J. Ma, *J. Mater. Chem. A*, 2018, **6,** 23478–23485.
13. T. Wang, L. Gao, P. Wang, X. Long, H. Chai, F. Li and J. Jin, *J. Colloid Interface Sci.*, 2022, **624,** 60–69.
14. D. Wang, P. Kanhere, M. Li, Q. Tay, Y. Tang, Y. Huang, T. C. Sum, N. Mathews, T. Sritharan and Z. Chen, *J. Phys. Chem. C*, 2013, **117,** 22894–22902.
15. M. S. Bakshi, *Cryst. Growth Des.*, 2016, **16,** 1104–1133.
16. C. Li, P. Wang, H. Li, M. Wang, J. Zhang, G. Qi and Y. Jin, *Nanoscale*, 2018, **10,** 14290–14297.
17. Y. Lu, Y. Yang, X. Fan, Y. Li, D. Zhou, B. Cai, L. Wang, K. Fan and K. Zhang, *Adv. Mater.*, 2022, **34,** 2108178.
18. M. Samadpour, *RSC Adv.*, 2018, **8,** 26056–26068.
19. L. Mao, H. Deng, M. Li and S. Shen, *Sci. China Mater.*, 2023, **66,** 603–613.
20. L. Gao, X. Long, S. Wei, C. Wang, T. Wang, F. Li, Y. Hu, J. Ma and J. Jin, *Chem. Eng. J.*, 2019, **378,** 122193.
21. T. S. Koh, P. Anushkkaran, W. S. Chae, H. H. Lee, S. H. Choi and J. S. Jang, *J. Energy Chem.*, 2023, **77,** 27–37.

22. J. Zhang, R. García-Rodríguez, P. Cameron and S. Eslava, *Energy Environ. Sci.*, 018, **11,** 2972–2984.
23. P. Y. Tang, L. J. Han, F. S. Hegner, P. Paciok, M. Biset-Peiró, H. C. Du, X. K. Wei, L. Jin, H. B. Xie, Q. Shi and T. Andreu, *Adv. Energy Mater.*, 2019, **9,** 1901836.
24. P. Tang, H. Xie, C. Ros, L. Han, M. Biset-Peiró, Y. He, W. Kramer, A. P. Rodríguez, E. Saucedo, J. R. Galán-Mascarós and T. Andreu, *Energy Environ. Sci.*, 2017, **10,** 2124–2136.
25. P. Dias, A. Vilanova, T. Lopes, L. Andrade and A. Mendes, *Nano Energy*, 2016, **23,** 70–79.
26. J. Xiao, C. Li, X. Jia, B. Du, R. Li and B. Wang, *J. Colloid Interface Sci.*, 2023, **633,** 555–565.
27. D. Chen and Z. Liu, *ChemSusChem*, 2018, **11,** 3438–3448.
28. Z. Sun, G. Fang, J. Li, J. Mo, X. He, X. Wang and Z. Yu, *Chem. Phys. Lett.*, 2020, **754,** 137736.
29. X. Zhao, C. Lu, S. Li, Y. Chen, G. Zhang, D. Zhang, K. Feng and J. Zhong, *J. Energy Chem.*, 2022, **69,** 414–420.
30. P. Wang, S. Wang, L. Gao, X. Long, H. Chai, F. Li, Q. Wang and J. Jin, *J. Catal.*, 2022, **413,** 398–406.
31. L. Gao, P. Wang, H. Chai, S. Li, J. Jin and J. Ma, *Nanoscale*, 2022, **14,** 17044–17052.
32. L. K. Dhandole, T. S. Koh, P. Anushkkaran, H. S. Chung, W. S. Chae, H. H. Lee, S. H. Choi, M. Cho and J. S. Jang, *Appl. Catal. B*, 2022, **315,** 121538.
33. L. K. Dhandole, P. Anushkkaran, W. S. Chae, H. S. Chung, H. H. Lee, S. H. Choi, M. Cho and J. S. Jang, *Chem. Eng. J.*, 2022, **446,** p.136957.
34. L. Wang, H. Hu, N. T. Nguyen, Y. Zhang, P. Schmuki, Y. Bi, *Nano Energy*, 2017, **35,** 171–178.
35. B. Chen, W. Fan, B. Mao, H. Shen, W. Shi, *Dalton Trans.*, 2017, **46,** 16050–16057.
36. B. Eftekharinia, A. Moshaii, N. Sobhkhiz Vayghan and A. Dabirian, *ChemCatChem*, 2018, **10,** 4665–4675.
37. Z. Xu, Z. Fan, Z. Shi, M. Li, J. Feng, L. Pei, C. Zhou, J. Zhou, L. Yang, W. Li, G. Xu, S. Yan, Z. Zou, *ChemSusChem*, 2018, **11,** 237–244.
38. A. Tofanello, A. L. Freitas, W. M. Carvalho Jr, T. Salminen, T. Niemi and F. L. Souza, *J. Phys. Chem. C*, 2020, **124,** 6171–6179.
39. Y. Fu, C. L. Dong, W. Zhou, Y. R. Lu, Y. C. Huang, Y. Liu, P. Guo, L. Zhao, W. C. Chou and S. Shen, *Appl. Catal. B*, 2020, **260,** 118206.
40. A. Z. Khan, T. N. Jahangir, T. A. Kandiel, K. Alhooshani and A. A. Al-Saadi, *Appl. Catal. A-Gen.*, 2022, **650,** 118979.